https://doi.org/10.1016/j.apenergy.2018.03.037

Modeling of all porous solid oxide fuel cells

Haoran Xu[1], Bin Chen[1], Peng Tan[1], Weizi Cai[1], Wei He[1], David Farrusseng[2*], Meng Ni[1,3*]

[1] Building Energy Research Group, Department of Building and Real Estate
The Hong Kong Polytechnic University, Hung Hom, Kowloon, Hong Kong, China
[2]Institut de Recherches sur la Catalyse et l'Environnement de Lyon, IRCELYON, Université
Lyon 1, CNRS. 2, Av. Albert Einstein F-69626, Villeurbanne, France
[3] Environmental Energy Research Group, Research Institute for Sustainable Urban
Development (RISUD), The Hong Kong Polytechnic University, Hung Hom, Kowloon, Hong
Kong, China

Abstract:

The all porous solid oxide fuel cell concept is proposed to solve the carbon deposition problem of solid oxide fuel cells. The transport of oxygen molecules from the cathode to the fuel side through the porous electrolyte can resist carbon deposition but could reduce the fuel cell performance. In this paper, a two-dimensional model for all porous solid oxide button cells is developed for the first time. After model validation with experimental data, the model is then extended for a tubular cell for parametric simulations. The effects of operating conditions and the electrolyte microstructure properties on carbon resistance and electrochemical performance of all porous solid oxide fuel cells are examined. The good carbon resistance of all porous solid oxide fuel cell is numerically demonstrated. It is found that the electrochemical performance and anode surface O/C ratio is significantly affected by anode inlet gas composition and flowrate. In addition, the anode supported all porous solid oxide fuel cell shows a great potential in terms of both power generation and coking resistance. The results of this study form a solid foundation to understand the mechanism and promising future of all porous solid oxide fuel cells.

Keywords: All porous solid oxide fuel cell; Methane coking; Carbon deposition; Mathematical modeling

---

* Corresponding authors:

Email: bsmengni@polyu.edu.hk; Tel: 852-27664152; Fax: 852-27645131 (NI M).

david.farrusseng@ircelyon.univ-lyon1.fr (David Farrusseng)

1. Introduction

A solid oxide fuel cell (SOFC) is one of the most attractive technology for converting the chemical energy fuels to electricity through electrochemical reactions [1-4]. Compared with other electric generators, SOFCs work in a clean, quiet and high efficiency manner. Compared with low temperature fuel cells such as proton exchange membrane fuel cells (PEMFCs) requiring very pure hydrogen fuel, SOFCs are fuel flexible and can use CO containing feeds for power generation. The utilization of carbon contained fuel in SOFCs has received more and more interest recently, including the direct utilization of solid carbon [5, 6]. Methane is an interesting alternative fuel choice for SOFCs as it is a main component in biogas and natural gas. Compared with H_2, methane has a higher volumetric energy density with lower price. Using methane as fuel can hopefully accelerate the commercialization of SOFCs for a variety of applications[7-11]. However, the direct fueling of methane causes severe coking and carbon deposition on SOFC anode (typically with nickel catalyst), resulting in catalyst deactivation[12]. Apart from designing novel anode materials [13, 14], strategies like adding external reformers and introducing steam together with methane have been proposed to enable nickel based anodes for the use of methane while resisting carbon deposition[15-17]. Nevertheless, these strategies require extra auxiliary facilities and raise the total expense.

Recently, Guo et al. [18] proposed a novel concept of all porous solid oxide fuel cell (AP-SOFC). By using a porous electrolyte, part of $\mathrm{O_2}$ from the cathode side can be transported to the fuel side to inhibit carbon deposition from methane fuel. In their preliminary experimental testing, the AP-SOFC consists of 2 mm thickness porous $\mathrm{Gd_{0.1}Ce_{0.9}O_{1.9}}$ (CGO) membrane as electrolyte, Ni-CGO and $Ba_{0.5}Sr_{0.5}Co_{0.8}Fe_{0.2}O_{3-\delta}$ (BSCF) as anode and cathode, respectively. With the Ohmic resistance accounting for nearly 98% of total resistance of the cell, the peak power density of the cell reaches 214, 156 and 94 W m^{-2} at 750, 700 and 600 °C, respectively. After a 2000 h stable operation in a CH_4-containing atmosphere without using an external reformer or steam addition, no carbon deposition on the anode is observed. After further reducing the thickness of the electrolyte from 2 mm to 112 μm in their very recent work [19], the same authors obtained 2140 W m^{-2} at 750 °C with a stable operation for more than 220 hours in the atmosphere of dry methane and dry propane. Their preliminary experimental studies clearly demonstrated the feasibility of the AP-SOFC using hydrocarbon fuels without carbon deposition under certain operating conditions for button cell configuration. However, it is still unclear how the microstructure of the electrolyte and how the operating conditions affect the carbon resistance and performance of the AP-SOFC, especially for a practical AP-SOFC with gas composition variation along the channels. To achieve good carbon resistance and cell performance in improved AP-SOFC design, a fundamental understanding of the coupled transport and reaction processes in AP-SOFC is essential.

Due to the transportation of gaseous O_2 from cathode to anode through the porous electrolyte, the reactions kinetics and mass/momentum transportations are much more complicated than traditional SOFCs with dense electrolyte. Apart from the electrochemical oxidization of H_2 and CO, methane oxidization reaction, methane steam reforming reaction, water gas shift reaction, H_2 and CO oxidization may co-exist in anode and other areas of the AP-SOFC. For the safe and high-performance operation of AP-SOFCs, it is urgent to understand these important reactions and the mass/momentum transportation phenomena of different gas species. To the best of authors' knowledge, all porous solid oxide fuel cells has not been modeled and simulated yet. To fill this research gap, the first mathematical model for AP-SOFC is developed and numerical simulations are conducted in the present paper. The model is validated by comparing the simulation results with experimental data and good agreement is observed.

2. Model description

2D mathematical models for AP-SOFCs are developed and fully considered the electrochemical reactions, chemical reactions, ion/electron conduction and mass/momentum transportation. The schematics of AP-SOFC is shown in Fig.1. The button cell has a surface area of 2.54 cm^{-2} with the thickness of its anode, electrolyte and cathode being 55 μm, 2 mm and 25 μm, respectively. The cell uses Ni-CGO composites as anode, CGO as electrolyte and BSCF as cathode. Material properties, chemical/electrochemical reaction kinetics and other tuning parameters are adopted and listed in Table 1 and Table 2, respectively.

In operation, CH_4 and O_2 are introduced into the anode and cathode respectively. Gaseous O_2 molecules diffuse through porous electrolyte into anode and react with CH_4 molecules to form CO_2 and H_2O. H_2O molecules will react with CH_4 molecules through methane steam reforming reaction and produce H_2 and CO molecules. Both H_2 and CO will participate in the electrochemical reaction with O^{2-} ions and generate H_2O and CO_2 on triple phase boundary (TPB) sites. Along with the generation of H_2O and CO_2, electrons are released and reaches the cathode through external circuit to generate electrical power and continue the electrochemical reaction. H_2 and CO will also react with O_2 to form H_2O and CO_2. Due to the existence of H_2O and CO, Water gas shift reaction catalyzed by nickel is also considered on anode.

2.1 Model assumption

(1) Both H_2 and CO participate in the electrochemical reactions and the TPB sites they shared is proportional to their local concentration percentage.

(2) TPB sites are distributed uniformly in the whole porous electrode. Both ionic- and electronic- conducting phases in the porous electrodes are homogeneous and continuous.

(3) Gases in the model ($CH_4, CO, CO_2, H_2O, H_2, N_2, O_2$) are ideal gases.

(4) Temperature distribution in the cell is uniform due to its small size.

2.2 Chemical reactions

Compared with conventional SOFCs, the chemical reactions occurred in AP-SOFCs are more complicated due to the transport of gaseous O_2 from cathode to anode. The existence of O_2 molecules on anode enables the chemical oxidization of CH_4 (R_{MO}), H_2 (R_{HO}), and CO (R_{CO}) as shown in Eq. (1) to Eq. (3).

$$CH_4 + 2O_2 = CO_2 + 2H_2O \qquad (1)$$

$$H_2 + 0.5O_2 = H_2O \qquad (2)$$

$$CO + 0.5O_2 = CO_2 \qquad (3)$$

H_2 and CO in Eq. (2) and Eq. (3) mainly comes from methane steam reforming reaction (R_{MSR}) as shown in Eq. (4).

$CH_4 + H_2O \leftrightarrow CO + 3H_2$ (4)

Due to the co-existence of H_2O and CO, water gas shift reaction (R_{WGSR}) catalyzed by nickel in the porous anode is also considered as shown in Eq. (5).

$CO + H_2O \leftrightarrow CO_2 + H_2$ (5)

Due to the all porous structure of the AP-SOFC, the above reactions are considered to be possible in the whole AP-SOFC. Their reaction rates are calculated using formulas summarized in Table 2.

2.3 Electrochemical reaction

Both H_2 and CO are considered to electrochemically react with O^{2-} and release electrons as shown in Eq. (6) and Eq. (7). The O^{2-} ions are formed in the cathode then transport through the electrolyte to the anode. Although electrochemical oxidation of CH_4 could take place in the SOFC anode, the reaction rate is much lower than that of H_2/CO electrochemical oxidation reaction. In addition, the CH_4 steam reforming reaction (Eq. 4) and chemical oxidation (Eq. 1) are fast enough for effective CH_4 conversion. Thus, in the present paper, only H_2 and CO electrochemical oxidation reactions are considered. The electrochemical reduction of O_2 (Eq. (8)) and oxidization of H_2 and CO are shown as follows.

$H_2 + O^{2-} = H_2O + 2e^-$ (6)

$CO + O^{2-} = CO_2 + 2e^-$ (7)

$O_2 + 4e^- = 2O^{2-}$ (8)

The overall electrochemical reactions of H_2 and CO as fuel and O_2 as oxidant are written as

Eq. (9) and Eq. (10).

$$H_2 + O_2 = H_2O \qquad (9)$$

$$CO + O_2 = CO_2 \qquad (10)$$

Equilibrium potentials (E_{eq}) for Eq. (9) and Eq. (10) can be calculated as follows.

$$E_{H_2} = E_{H_2}^0 + \frac{RT}{2F} \ln \left[\frac{P_{H_2}^L (P_{O_2}^L)^{1/2}}{P_{H_2O}^L} \right] \qquad (11)$$

$$E_{CO} = E_{CO}^0 + \frac{RT}{2F} \ln \left[\frac{P_{CO}^L (P_{O_2}^L)^{1/2}}{P_{CO_2}^L} \right] \qquad (12)$$

Here R is the universal gas constant, T is the operating temperature, F is the Faraday constant. $E_{H_2}^0$ and E_{CO}^0 are the respective standard potentials for Eq. (9) and Eq. (10). $P_{H_2}^L$, $P_{H_2O}^L$, P_{CO}^L and $P_{CO_2}^L$ are the anode local gas partial pressures for H_2, H_2O, CO and CO_2, respectively. $P_{O_2}^L$ is the cathode O_2 local partial pressure. The values of E_{CO}^0 and $E_{H_2}^0$ at given temperature can be calculated by Eq. (13) and Eq. (14):

$$E_{H_2}^0 = 1.253 - 0.00024516T \text{ (V)} \qquad (13)$$

$$E_{CO}^0 = 1.46713 - 0.0004527T \text{ (V)} \qquad (14)$$

It should be noted that the equilibrium potentials calculated by Eq. (11) and Eq. (12) are equal at an open circuit condition. When current is extracted from AP-SOFC, the equilibrium potentials for these two reactions become different due to the different overpotential losses involved in electrochemical oxidation of H_2 and CO.

The operating potential can be calculated by deducting overpotential losses from equilibrium potential as shown in Eq. (15) [5, 20]:

$$V = E_{eq} - \eta_{act} - \eta_{ohmic} \qquad (15)$$

The activation overpotential loss (η_{act}) stems from the activation barrier of the electrochemical reactions at the electrodes. This overpotential is strongly related with the reactions at hand, the electrode material and its microstructure. η_{act} can be described by Butler-Volmer equation as shown in Eq. (16).

$$i = i_0 \left\{ \exp\left(\frac{\alpha n F \eta_{act}}{RT}\right) - \exp\left(\frac{(1-\alpha) n F \eta_{act}}{RT}\right) \right\} \qquad (16)$$

Here i and i_0 are the operating current density and exchange current density, respectively. α is the electron transfer coefficient and n is the number of transferred electrons per electrochemical reaction. i_0 can be expressed as Eq. (17).

$$i_0 = \gamma \exp\left(-\frac{E_{act}}{RT}\right) \qquad (17)$$

Here γ is the pre-exponential factor and E_{act} is the activation energy.

The ohmic overpotential (η_{ohmic}) is caused by ionic/electronic resistance in the cell. It can be calculated by Ohm law. It should be noted that the mass-transport-related overpotential loss is already considered by using local gas partial pressure in equilibrium potential calculation in Eqs. (11) and (12). The electrochemical reaction parameters can be found in Table 3.

2.4 Mass and momentum transport

Mass transport of gas species in channels and porous materials is calculate by extended Fick's as shown in Eq. (18)[21]:

$$N_i = -\frac{1}{RT}\left(\frac{B_0 y_i P}{\mu}\nabla P - D_i^{eff}\nabla(y_i P)\right) \; (i = 1, \ldots, n) \qquad (18)$$

Here B_0 is the porous material permeability and μ is the gas viscosity. y_i and D_i^{eff} are the mole fraction and overall effective diffusion coefficient of component i, respectively. D_i^{eff} is determined by both molecular diffusion coefficient (D_{im}^{eff}) and Knudsen diffusion coefficient

($\mathrm{D_{ik}^{eff}}$) as shown in Eq. (19) [22]:

$$\mathrm{D_i^{eff}} = \frac{\varepsilon}{\tau}\left(\frac{1}{\mathrm{D_{im}^{eff}}} + \frac{1}{\mathrm{D_{ik}^{eff}}}\right)^{-1} \qquad (19)$$

Here ε is the porosity and τ is the tortuosity factor. Detailed calculation of $\mathrm{D_{im}^{eff}}$ and $\mathrm{D_{ik}^{eff}}$ can be found in ref. [23].

The mass conservation can be described by Eq. (20) as:

$$\nabla\left(-\mathrm{D_i^{eff}}\nabla \mathrm{c_i}\right) = \mathrm{R_i} \qquad (20)$$

where $\mathrm{c_i}$ is the gas molar concentration and $\mathrm{R_i}$ is the mass source term of the gaseous species.

Momentum transport of gas species in channels and porous material is calculated by Navier-Stokes equation with Darcy’s term as shown in Eq. (21):

$$\rho\frac{\partial u}{\partial t} + \rho u\nabla u = -\nabla p + \nabla\left[\mu\left(\nabla u + (\nabla u)^{T}\right) - \frac{2}{3}\mu\nabla u\right] - \frac{\varepsilon\mu u}{k} \qquad (21)$$

Here ρ is the gas density and u is the velocity vector.

2.5 Boundary conditions and model solution

Electric potentials are specified at the outlet surface of two electrodes while the two ends along the cell length are electrically insulated. Inflow gas flow rate and molar fraction of the species are given at the channel inlets. Zero flux is specified at the end of the electrodes and electrolyte. Pressure condition is specified at the gas channel outlets.

The model is solved at given parameters such as operating temperature, voltage, inlet gas flow rate and species mole fraction. The commercial software COMSOL MULTIPHYSICS® is employed for the numerical simulation.

3 Results and discussion

3.1 Model validation

In the experiments [18], all porous planar SOFCs (electrolyte-supported) were prepared and tested at 700 ℃ for 2000 hours. During the test, there was neither any CH_4 on the cathode side nor CO_x on the anode side observed by online gas chromatography. And no carbon deposition was observed after the test.

In accordance with the experiments, the all porous SOFC for model validation employed Ni-CGO anode, CGO electrolyte and BSCF cathode with the same structural parameters in ref.[18]. The model is validated by comparing the simulation I-V characteristics with experimental data as shown in Fig. 2a with high accuracy. The same tuning parameters are used in the subsequent parametric simulations. The structure is extended to a tubular AP-SOFC cell for the study of practical operation. An anode supported AP-SOFC is also designed and analyzed in this study.

3.2 Analysis of carbon deposition resistance characteristic and safety operation

The AP-SOFC has shown excellent resistance to methane coking and carbon deposition in the experiments [18, 19]. According to fuel cell handbook[24], methane coking can be avoided at high oxygen-to-carbon ratio (O/C ratio). The O/C ratio here is based on the total atoms of oxygen in the steam and air feed, i.e., one mole O_2 and one mole H_2O provides two moles and one mole oxygen atoms, respectively. Moreover, for the whole nickel deposition area, anode surface has the lowest oxygen and steam fraction while the highest methane fraction.

Thus, 1.5 O/C ratio at anode surface is suggested to be a minimum safe operation O/C ratio for AP-SOFCs in this paper.

The AP-SOFC button cell exhibits a high (~ 3) and uniform O/C ratio at different operating potentials on anode surface as shown in Fig. 2b. A smaller operating voltage brings a faster electrochemical reaction and produces more H_2O, hence a lager O/C ratio can be obtained.

The distributions of different gas species are also given in Fig. 2c. Although the porous electrolyte allows the transportation of gas species between anode and cathode, the molar fraction of methane in cathode and oxygen in anode is close to zero due to the fast consumption by chemical and electrochemical reactions. For safety operation, the concentration of H_2 and CO in air in suggested to be smaller than the “Lower Explosive or Flammable Limit”, which are 4% and 12%, respectively. Therefore, the $H_2 \times O_2$ and $CO \times O_2$ products should be smaller than 8.4×10^{-3} and 2.52×10^{-2}, respectively. As can be seen in Fig. 2d, the good separation between fuels and oxygen results in a quite low fuel×oxygen product in the whole test area with a maximum value of 1.2×10^{-4} , which ensures a safe operating environment. It should also be noted that the electrodes have a higher porosity (0.6) than electrolyte (0.42), which is in consistence with the experiments. The use of higher electrode porosity minimizes the gas transport effect in the porous electrodes, thus the analyses can focus on how the porous electrolyte can affect the gas transport between the cathode channel and the anode channel.

3.3 Effect of cathode inlet O_2 molar fraction

In the experiment conducted by Guo et al, because of laboratory safety instructions, a low molar fraction of O_2 (4%) was used in an AP-SOFC button cell in small effective reaction area. Whereas in practical operation, air will be employed in much larger tubular SOFC. Therefore, a tubular AP-SOFC model is here developed with the same governing equations applied in the previous button AP-SOFC. The tubular cell has a length of 18 mm, an inner diameter of 10 mm and an outer diameter of 14.16 mm. The thickness and micro-structure of the tubular cell are the same with the button cell. The methane molar fraction at the anode inlet is 4 %. The performances of tubular AP-SOFCs with different cathode inlet O_2 molar fraction (4% and 21%) are compared to evaluate the AP-SOFC performance in practical operation.

The higher O_2 molar fraction in air indeed changes the electrochemical performance of the tubular AP-SOFC as shown in Fig. 3a due to the significant decrease of syngas $(H_2 + CO)$ concentration presented in Fig. 3b. With the increase of cathode inlet O_2 molar fraction from 4% to 21%, the maximum output power density drops from 136 W m^{-2} to 96 W m^{-2}. This is mainly caused by the low syngas concentration level produced from small methane molar fraction (4%) and fast chemical oxidation reaction. As can be seen from Fig. 3b, the peak syngas molar fraction decreases from 0.9 % to 0.3 % when cathode O_2 molar fraction is increased from 4 % to 21%, indicating that a higher inlet methane concentration may be needed. The detailed O_2 distribution inside the porous anode-electrolyte-cathode area at the inlet and outlet of tubular AP-SOFC is also shown in Fig. 3c. At the inlet area, there is a significant O_2 molar fraction gradient while the distribution of O_2 is quite uniform at the outlet. In addition to electrochemical performance, O/C ratio is significantly affected by cathode inlet O_2 molar fraction. As can be found in Fig. 4a and Fig. 4b, the average anode surface O/C ratio rises from ~ 3.4 to ~ 260 as the cathode inlet O_2 molar fraction is increased from 4 % to 21 %. Furthermore, the anode surface O/C-ratio distribution gradient in tubular AP-SOFC is rather steep（Fig. 4c and 4d） compared with that in button AP-SOFC (Fig. 2b). This difference is mainly caused by the different cell sizes and flow directions in these two kinds of AP-SOFCs. Due to the highest methane concentration at the anode inlet and relatively slow O_2 diffusion from cathode to anode through the porous electrolyte, the O/C-ratio is close to 0 at anode inlet. With the continuous consumption of methane and production of H_2O, the contribution by H_2O to O/C-ratio is increased along the cell length and becomes the crucial factor at low O_2 molar fraction (4 %) condition. For comparison, the O/C-ratio contributed by O_2 dominates at high O_2 molar fraction (21 %) condition. An important benefit brought by high cathode inlet O_2 molar fraction is the remarkably narrowed low-O/C -ratio region (O/C <1.5), which declines from 19 % to 1 % as the cathode inlet O_2 molar fraction is increased from 4 % to 21 %. Such a large high-O/C -ratio region fraction (> 99%) can effectively prevent AP-SOFCs from methane coking and carbon deposition.

3.4 Effect of anode inlet CH_4 molar fraction

Anode inlet CH_4 molar fraction is a key parameter for AP-SOFCs because it significantly affects both the O/C ratio and the electrochemical performance.

As shown in Fig. 5a, the current density rises quickly from 207 A m^{-2} to 362 A m^{-2} when the anode inlet CH_4 molar fraction is increased from 0.04 to 0.2. A further increase of current density can also be obtained with higher anode inlet CH_4 molar fraction, however, the anode surface average O/C-ratio decreases to be less than 1.5 when the anode inlet CH_4 molar fraction is higher than 0.32. For this reason, a too high anode inlet CH_4 molar fraction is not suggested to resist carbon deposition under the current simulation conditions. The high O/C-ratio at small anode inlet CH_4 molar fraction is mainly contributed by the O_2 (Fig. 5b), while H_2O dominants O/C ratio at large (> 0.15) anode inlet CH_4 molar fraction.

The CH_4 conversion efficiency is acceptable at different inlet fractions. With increasing anode inlet CH_4 molar fraction to 1.0, the conversion efficiency decreases from ~ 100 % to be about 53 %. For the suggested operation condition where the O/C-ratio and power density are both high (e.g. 0.2 anode inlet CH_4 molar fraction), the CH_4 conversion efficiency reaches 92 %. Besides, a high inlet CH_4 molar fraction also results in high concentration of syngas at the cell outlet (Fig. 5d), indicating the potential of syngas and electricity co-generation in the AP-SOFCs.

3.5 Effect of support layer type

Compared with the electrolyte-supported SOFC, an anode-supported SOFC has a thicker anode but much thinner electrolyte. In general, the anode concentration loss is negligibly small even in anode-supported SOFC while the ohmic loss from the electrolyte usually dominates the total overpotential losses in an electrolyte-supported SOFC. The use of anode-support can significantly reduce the total overpotential loss due to the substantially reduced electrolyte ohmic loss. In addition, as the catalytic sites for methane reforming reaction is restricted in anode, the anode-supported AP-SOFC shall provide a larger catalytic reaction area. The anode-supported AP-SOFC in the following parametric studies is designed to have the same material and length with the electrolyte-supported AP-SOFC, while the thickness of anode and electrolyte are designed to be 500 μm and 100 μm, respectively.

The significant improvement of output power density has been shown in Fig. 6a. The peak power density has been elevated from 146 W m^{-2} in an electrolyte-supported AP-SOFC to 1607 W m^{-2} in an anode-supported AP-SOFC.

As for the electrochemical performance (Fig. 6b), the electrochemical reaction rate grows quickly with increasing anode inlet CH_4 molar fraction at a relatively low CH_4 molar fraction (< 0.2), however it climbs slowly with the further increase of CH_4 molar fraction but drops slightly at large CH_4 molar fraction (> 0.34). On the other hand, the O/C-ratio falls continuously with increasing CH_4 molar fraction. Compared with electrolyte-supported AP-SOFC, the anode-supported AP-SOFC has a much better carbon deposition resistance as the O/C-ratio keeps at a high value (~ 5) at the high (0.36) anode inlet CH_4 molar fraction condition as shown in Fig. 6c. It can also be found from Fig. 6d that anode-supported AP-SOFC also provides a very high CH_4 conversion efficiency (> 97 %) in the range of studied parameters, indicating a great economic advantage in large scale operation.

4 Conclusion

Mathematical models of all porous solid oxide fuel cells are developed to study their characteristics in preventing carbon deposition and outputting power density. The model is validated by experimental data. Key parameters affecting carbon deposition and electrochemical performance such as O/C-ratio and electrochemical reaction rate are investigated. The electrolyte-supported and anode-supported all porous solid oxide fuel cells are also compared to examine how support-type affects the carbon deposition resistance and power generation characteristics.

The diffusion of O_2 from cathode to anode significantly raises the O/C-ratio on anode electrode, which efficiently inhibits the methane coking and carbon deposition. A peak power density of 146 W m^{-2} has been obtained in an electrolyte-supported all porous solid oxide fuel cell with 100 SCCM air and 20 % CH_4 as cathode and anode inlet gas, respectively. The output power can be further improved to 1607 W m^{-2} in an anode-supported all porous solid oxide fuel cell at the same operating conditions with a higher O/C-ratio, showing a great potential in both power harvest and carbon resistance in this design.

It is also found that the CH_4 conversion efficiency is quite high and there is a rich rest of syngas in anode outlet. Therefore, it is possible for an all porous solid oxide fuel cell to efficiently cogenerate electricity power and syngas using methane without carbon deposition.

When all porous solid oxide fuel is extended to a larger scale, it can be a promising method in the utilization of methane for electricity generation and high-quality fuel conversion in real application. It should be noted that the support-type design is a preliminary work in optimizing all porous solid oxide fuel cells. Considering the very high O/C-ratio on most anode area of the investigated all porous solid oxide fuel cells, a further optimization on porous electrode and electrolyte is still possible.

Acknowledgement

This research is supported by a grant (F-PolyU501/15) from Research Grant Council (France/HK Joint Research Scheme), University Grants Committee, Hong Kong SAR, a grant from Environment and Conservation Fund (ECF 54/2015), Hong Kong SAR, and a grant from Research Institute for Sustainable Urban Development (RISUD) (1-ZVEA).

Nomenclature

Abbreviation

AP-SOFC	All porous solid oxide fuel cell
BSCF	Barium strontium cobalt ferrite ($Ba_{0.5}Sr_{0.5}Co_{0.8}Fe_{0.2}O_{3-\delta}$)
CGO	gadolinium-doped ceria ($Gd_{0.1}Ce_{0.9}O_{1.9}$)
CMO	Carbon monoxide oxidization
HO	Hydrogen oxidization
MO	Methane oxidization
MSR	Methane steam reforming
O/C	Oxygen to carbon
SCCM	Standard cubic centime per minute
SOFC	Solid oxide fuel cell
TPB	Triple phase boundary
WGS	Water gas shift

Roman

B_0	Permeability coefficient, m^2
c_{CO_2}	Mole concentration of carbon dioxide, mol·m^{-3}
c_{H_2O}	Mole concentration of water, mol·m^{-3}
D_i^{eff}	Effective diffusivity of species i , m^2·s^{-1}
D_{ik}^{eff}	Knudsen diffusion coefficient of i , m^2·s^{-1}
D_{im}^{eff}	Molecular diffusion coefficient of i, m^2·s^{-1}
E_{act}	Activation energy, J·mol^{-1}
E_{CO}	Equilibrium potential for carbon monoxide oxidization, V
E_{CO}^0	Standard equilibrium potential for carbon monoxide oxidization, V
E_{eq}	Equilibrium Nernst potential, V
E_{H_2}	Equilibrium potential for hydrogen oxidization, V
$E_{H_2}^0$	Standard equilibrium potential for hydrogen oxidization, V
F	Faraday constant, 96485 C·mol^{-1}
i	Operating current density, A·m^{-2}
i_o	Exchange current density, A·m^{-2}
n	Number of electrons transferred per electrochemical reaction
N_i	Flux of mass transport, kg·m^{-3}·s^{-1}
p	(partial) Pressure, Pa
P_{CO}^L	Local CO partial pressures, Pa
$P_{CO_2}^L$	Local CO_2 partial pressures, Pa

$P_{H_2}^{L}$	Local H_2 partial pressures, Pa
$P_{H_2O}^{L}$	Local H_2O partial pressures, Pa
$P_{O_2}^{L}$	Local O_2 partial pressures, Pa
R	Gas constant, 8.314 J·mol^{-1}·K^{-1}
R_{CMO}	Carbon monoxide oxidization reaction
R_{HO}	Hydrogen oxidization reaction
R_{MSR}	Methane steam reforming reaction
R_{MO}	Methane oxidization reaction
R_{WGS}	Water gas shift reaction
T	Temperature, K
u	Velocity field, m^3·s^{-1}
V	Volume fraction
y_i	Mole fraction of component i
z	Gas diffusion direction

Greek letters

α	Charge transfer coefficient
ε	Porosity
η_{act}	Activation overpotential loss, V
η_{ohmic}	Ohmic overpotential loss, V
κ	Permeability, m^2

μ	Dynamic viscosity of fluid, Pa·s
ρ	Fluid density, kg·m^{-3}
σ	Conductivity, S/m
γ	Pre-exponential factor, A m^{-2}
τ	Tortuosity

Reference

[1] Park S, Vohs JM, Gorte RJ. Direct oxidation of hydrocarbons in a solid-oxide fuel cell. Nature. 2000;404:265-7.

[2] Ormerod RM. Solid oxide fuel cells. Chemical Society Reviews. 2003;32:17-28.

[3] Singhal SC. Advances in solid oxide fuel cell technology. Solid State Ionics. 2000;135:305-13.

[4] Minh NQ. Solid oxide fuel cell technology—features and applications. Solid State Ionics. 2004;174:271-7.

[5] Xu H, Chen B, Liu J, Ni M. Modeling of direct carbon solid oxide fuel cell for CO and electricity cogeneration. Applied Energy. 2016;178:353-62.

[6] Yan M, Zeng M, Chen Q, Wang Q. Numerical study on carbon deposition of SOFC with unsteady state variation of porosity. Applied Energy. 2012;97:754-62.

[7] Gür TM. Comprehensive review of methane conversion in solid oxide fuel cells: Prospects for efficient electricity generation from natural gas. Progress in Energy and Combustion Science. 2016;54:1-64.

[8] Wang Y, Liu T, Fang S, Xiao G, Wang H, Chen F. A novel clean and effective syngas production system based on partial oxidation of methane assisted solid oxide co-electrolysis process. Journal of Power Sources. 2015;277:261-7.

[9] Buonomano A, Calise F, d'Accadia MD, Palombo A, Vicidomini M. Hybrid solid oxide fuel cells–gas turbine systems for combined heat and power: A review. Applied Energy. 2015;156:32-85.

[10] Xie Y, Ding H, Xue X. Direct methane fueled solid oxide fuel cell model with detailed reforming reactions. Chemical Engineering Journal. 2013;228:917-24.

[11] Ni M. Electrolytic effect in solid oxide fuel cells running on steam/methane mixture. Journal of Power Sources. 2011;196:2027-36.

[12] Li K, Jia L, Wang X, Pu J, Chi B, Li J. Enhanced methane steam reforming activity and electrochemical performance of Ni0.9Fe0.1-supported solid oxide fuel cells with infiltrated Ni-TiO2 particles. Scientific Reports. 2016;6:35981.

[13] Li M, Hua B, Pu J, Chi B, Jian L. Electrochemical performance and carbon deposition

resistance of M-BaZr0.1Ce0.7Y0.1Yb0.1O3-δ (M = Pd, Cu, Ni or NiCu) anodes for solid oxide fuel cells. Scientific Reports. 2015;5:7667.

[14] Myung J-h, Kim S-D, Shin TH, Lee D, Irvine JTS, Moon J, et al. Nano-composite structural Ni-Sn alloy anodes for high performance and durability of direct methane-fueled SOFCs. Journal of Materials Chemistry A. 2015;3:13801-6.

[15] Nguyen VN, Deja R, Peters R, Blum L. Methane/steam global reforming kinetics over the Ni/YSZ of planar pre-reformers for SOFC systems. Chemical Engineering Journal. 2016;292:113-22.

[16] Fu Q, Freundt P, Bomhard J, Hauler F. SOFC Stacks Operating under Direct Internal Steam Reforming of Methane. Fuel Cells. 2017;17:151-6.

[17] Liso V, Olesen AC, Nielsen MP, Kær SK. Performance comparison between partial oxidation and methane steam reforming processes for solid oxide fuel cell (SOFC) micro combined heat and power (CHP) system. Energy. 2011;36:4216-26.

[18] Guo Y, Bessaa M, Aguado S, Steil MC, Rembelski D, Rieu M, et al. An all porous solid oxide fuel cell (SOFC): a bridging technology between dual and single chamber SOFCs. Energy & Environmental Science. 2013;6:2119-23.

[19] Guo YM, Largiller G, Guizard C, Tardivat C, Farrusseng D. Coke-free operation of an all porous solid oxide fuel cell (AP-SOFC) used as an O2 supply device. Journal of Materials Chemistry A. 2015;3:2684-9.

[20] Xu H, Chen B, Ni M. Modeling of Direct Carbon-Assisted Solid Oxide Electrolysis Cell (SOEC) for Syngas Production at Two Different Electrodes. Journal of The Electrochemical Society. 2016;163:F3029-F35.

[21] Suwanwarangkul R, Croiset E, Fowler MW, Douglas PL, Entchev E, Douglas MA. Performance comparison of Fick's, dusty-gas and Stefan–Maxwell models to predict the concentration overpotential of a SOFC anode. Journal of Power Sources. 2003;122:9-18.

[22] Chan SH, Khor KA, Xia ZT. A complete polarization model of a solid oxide fuel cell and its sensitivity to the change of cell component thickness. Journal of Power Sources. 2001;93:130-40.

[23] Todd B, Young JB. Thermodynamic and transport properties of gases for use in solid oxide fuel cell modelling. Journal of Power Sources. 2002;110:186-200.

[24] NETL. Fuel Cell Handbook, Seventh Edition. DOE/NETL; 2004. p. CD.

[25] Shi Y, Cai N, Li C, Bao C, Croiset E, Qian J, et al. Modeling of an anode-supported Ni–YSZ|Ni–ScSZ|ScSZ|LSM–ScSZ multiple layers SOFC cell: Part I. Experiments, model development and validation. Journal of Power Sources. 2007;172:235-45.

[26] Luo Y, Shi Y, Li W, Cai N. Comprehensive modeling of tubular solid oxide electrolysis cell for co-electrolysis of steam and carbon dioxide. Energy. 2014;70:420-34.

[27] Jin W, Gu X, Li S, Huang P, Xu N, Shi J. Experimental and simulation study on a catalyst packed tubular dense membrane reactor for partial oxidation of methane to syngas. Chemical Engineering Science. 2000;55:2617-25.

[28] Ni M, Leung DYC, Leung MKH. Electrochemical modeling and parametric study of methane fed solid oxide fuel cells. Energ Convers Manage. 2009;50:268-78.

[29] Ni M. 2D heat and mass transfer modeling of methane steam reforming for hydrogen

production in a compact reformer. Energy Conversion and Management. 2013;65:155-63.

[30] Ni M. Modeling of SOFC running on partially pre-reformed gas mixture. International Journal of Hydrogen Energy. 2012;37:1731-45.

[31] Xu H, Chen B, Zhang H, Sun Q, Yang G, Ni M. Modeling of direct carbon solid oxide fuel cells with H2O and CO2 as gasification agents. International Journal of Hydrogen Energy. 2017;42:15641-51.

[32] Xu H, Chen B, Irvine J, Ni M. Modeling of CH4-assisted SOEC for H2O/CO2 co-electrolysis. International Journal of Hydrogen Energy. 2016;41:21839-49.

List of Tables

Table 1 Material properties

Parameters	**Value or expression**	**Unit**
Conductivity		
Porous CGO	$0.224 \times e^{\frac{16054}{RT}}$ [18]	S m^{-1}
BSCF	$-24455 + 82.321T - \frac{8.28T^2}{1000} + \frac{2.7778T^3}{10000}$ [18]	S m^{-1}
Ni	$3.27 \times 10^6 - 1065.3T$ [25]	S m^{-1}
Porosity		
Cathode	0.6 [18]	
Anode	0.6 [18]	
Electrolyte	0.42 [18]	
Anode volume fraction		
CGO	0.23 [18]	
Ni	0.77 [18]	
Cathode volume fraction		
CGO	0.25 [18]	
BSCF	0.75 [18]	
$\mathbf{S_{TPB}}$	2.14×10^5 [26]	m^2/m^3
Electrode tortuosity	3	

Table 2 Chemical reaction parameters

Reaction	**Unit**
Methane oxidization reaction rate [27]	
$5 \times 10^4 \times e^{\frac{-166000}{RT}} \times p_{CH_4} \times p_{O_2}$ (anode)	$mol\, m^3\, s^{-1}$
$1.1 \times e^{\frac{-166000}{RT}} \times p_{CH_4} \times p_{O_2}$ (other area)	$mol\, m^3\, s^{-1}$
Hydrogen oxidization reaction rate [27]	
$5 \times 10^4 \times e^{\frac{-48484}{RT}} \times p_{CH_4} \times p_{O_2}^{0.5}$	$mol\, m^3\, s^{-1}$
Carbon monoxide oxidization reaction rate [27]	
$5 \times 10^4 \times e^{\frac{-47773}{RT}} \times p_{CO} \times p_{O_2}^{0.5}$	$mol\, m^3\, s^{-1}$
Methane steam reforming reaction rate [28]	
$2.395 \times 10^7 \times e^{\frac{-231266}{RT}} \times (p_{CH_4} \times p_{H_2O} - \frac{p_{CH_4}^3 \times p_{CO}}{K_{pr}})$	$mol\, m^3\, s^{-1}$
$K_{pr} = 1.0267 \times 10^{10} \times e^{-0.2513 \times Z^4 + 0.3665 \times Z^3 + 0.5810 \times Z^2 - 27.134 \times Z + 3.277}$	
$Z = \frac{T}{1000}$	
Water gas shift reaction rate [29]	
$0.0171 \times e^{\frac{-103191}{RT}} \times (p_{CO} \times p_{H_2O} - \frac{p_{H_2} \times p_{CO_2}}{k_{ps}})$	$mol\, m^3\, s^{-1}$
$k_{ps} = e^{-0.2935 \times Z^3 + 0.6351 \times Z^2 + 4.1788 \times Z + 0.0169}$	
$Z = \frac{T}{1000}$	

Table 3 Electrochemical reaction parameters

Parameter	**Value**	**Unit**
γ_{H_2}	3.68×10^9 [30]	A m^{-2}
E_{act,H_2}	1.2×10^5 [30]	J mol^{-1}
γ_{O_2}	1.39×10^{10} [30]	A m^{-2}
E_{act,O_2}	1.2×10^5 [30]	J mol^{-1}
γ_{CO}	1.67×10^9 [31]	A m^{-2}
$E_{act,CO}$	1.2×10^5 [31]	J mol^{-1}
α_{H_2}	0.5 [30]	
α_{CO}	0.5 [32]	
α_{O_2}	0.5 [32]	

List of Figures

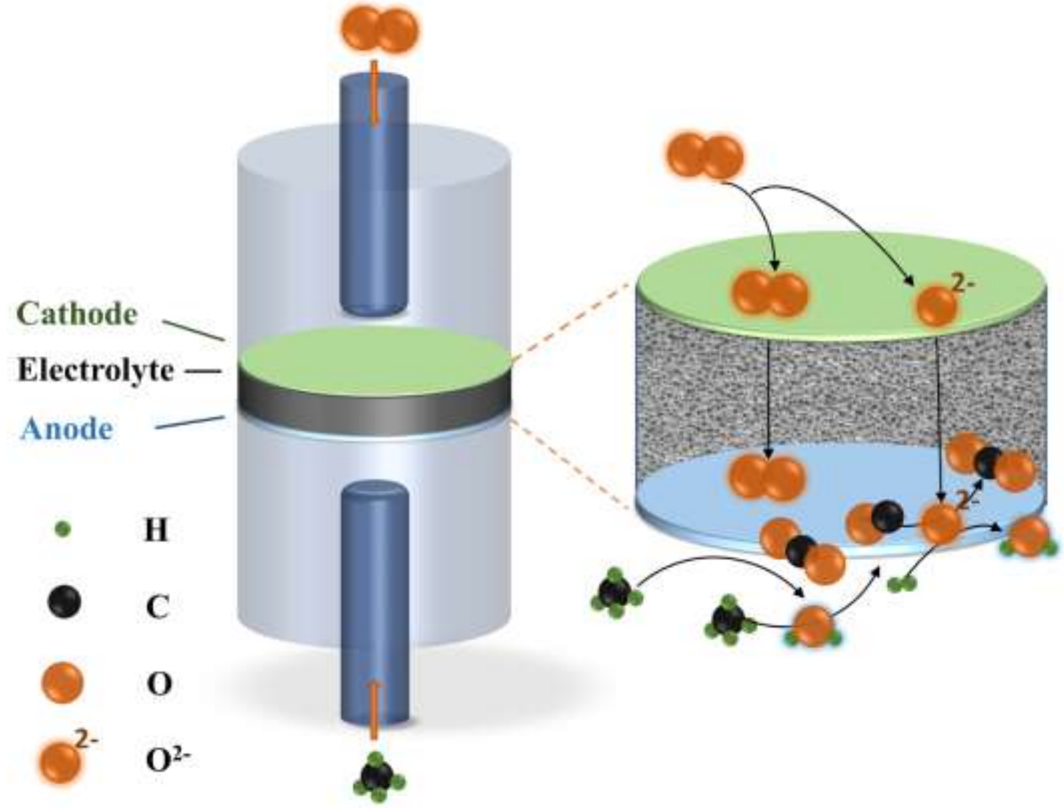

Fig.1 Schematic of a tubular all porous solid oxide fuel cell (AP-SOFC)

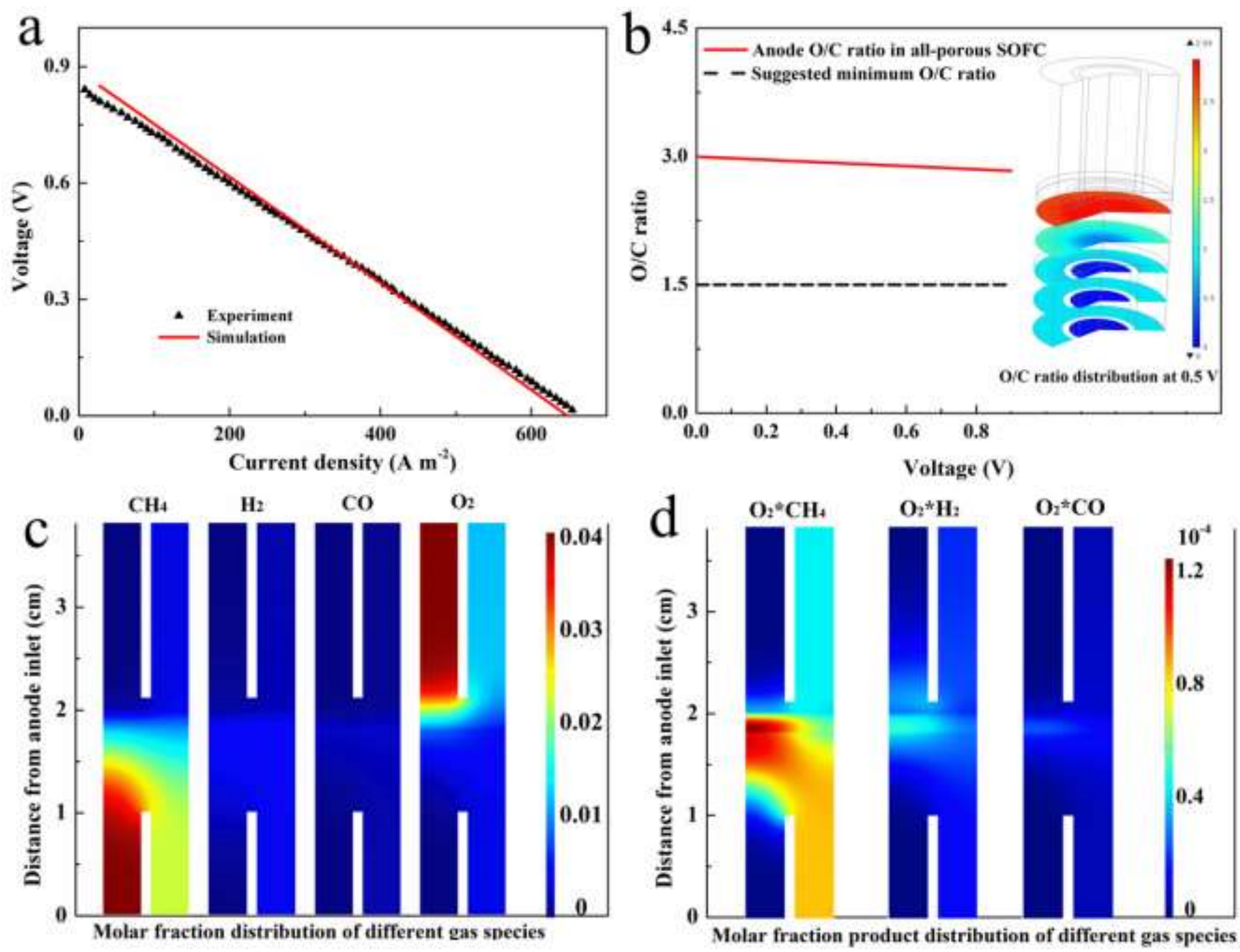

Fig. 2 (a)Model validation for AP-SOFCs; (b) Anode surface O/C ratio of the button AP-SOFC at different voltages;(c) Molar fraction distribution of CH_4, H_2, CO and O_2 in the whole cell area at 0.5 V operating potential; (d) Molar fraction product distribution of oxygen and different fuels in the whole cell area at 0.5 V operating potential.

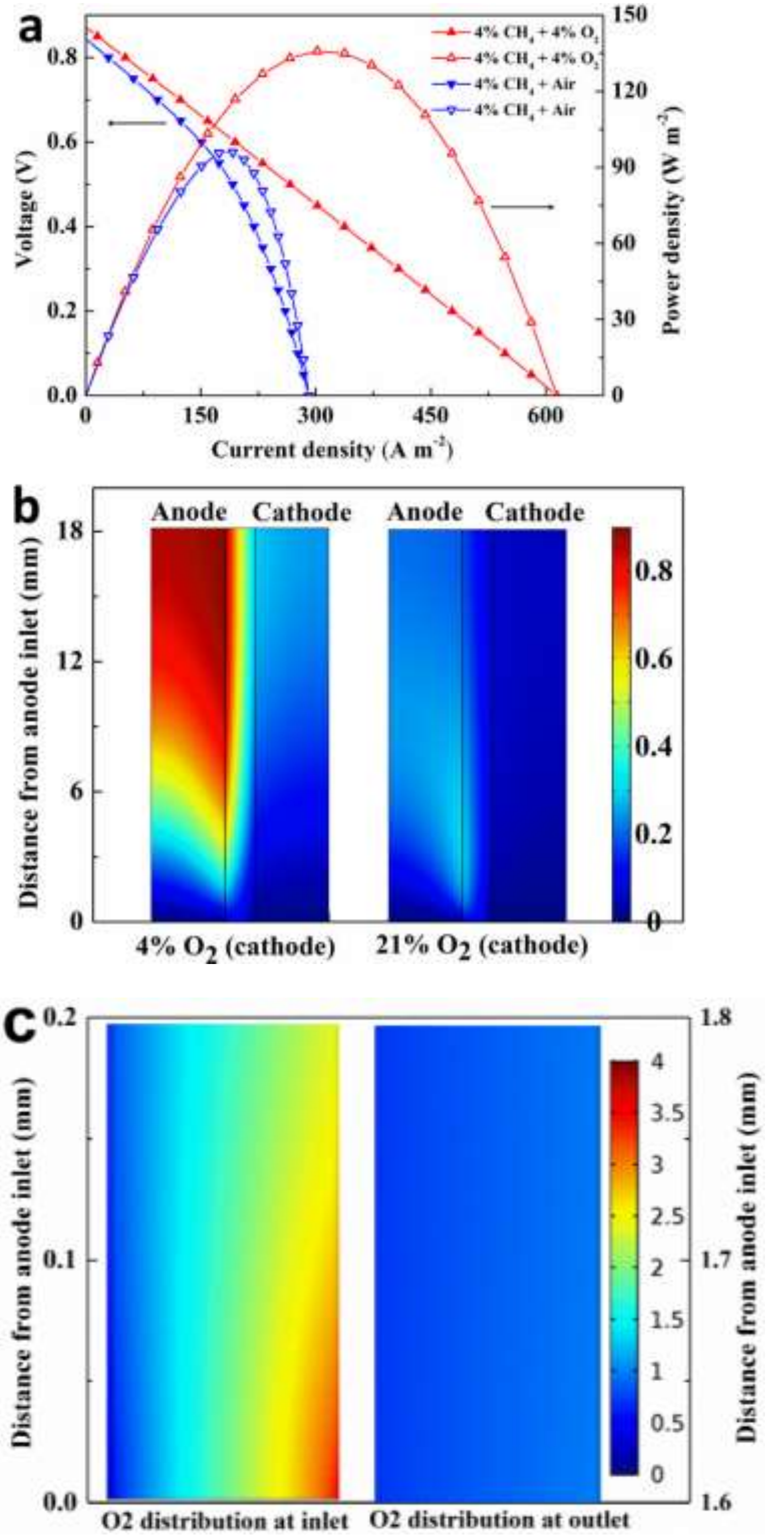

Fig. 3 (a) I-V-P curves of the tubular all-porous SOFC, (b) Syngas (CO+H_2) molar percentage (%) distribution in the tubular all-porous SOFC at 0.8V with 4 % CH_4 in anode inlet gas, 4 % and 21 % O_2 in cathode inlet gas, respectively and (c) O_2 molar percentage (%) distribution at inlet and outlet of the tubular all-porous SOFC at 0.8V with 4 % CH_4 at the anode inlet.

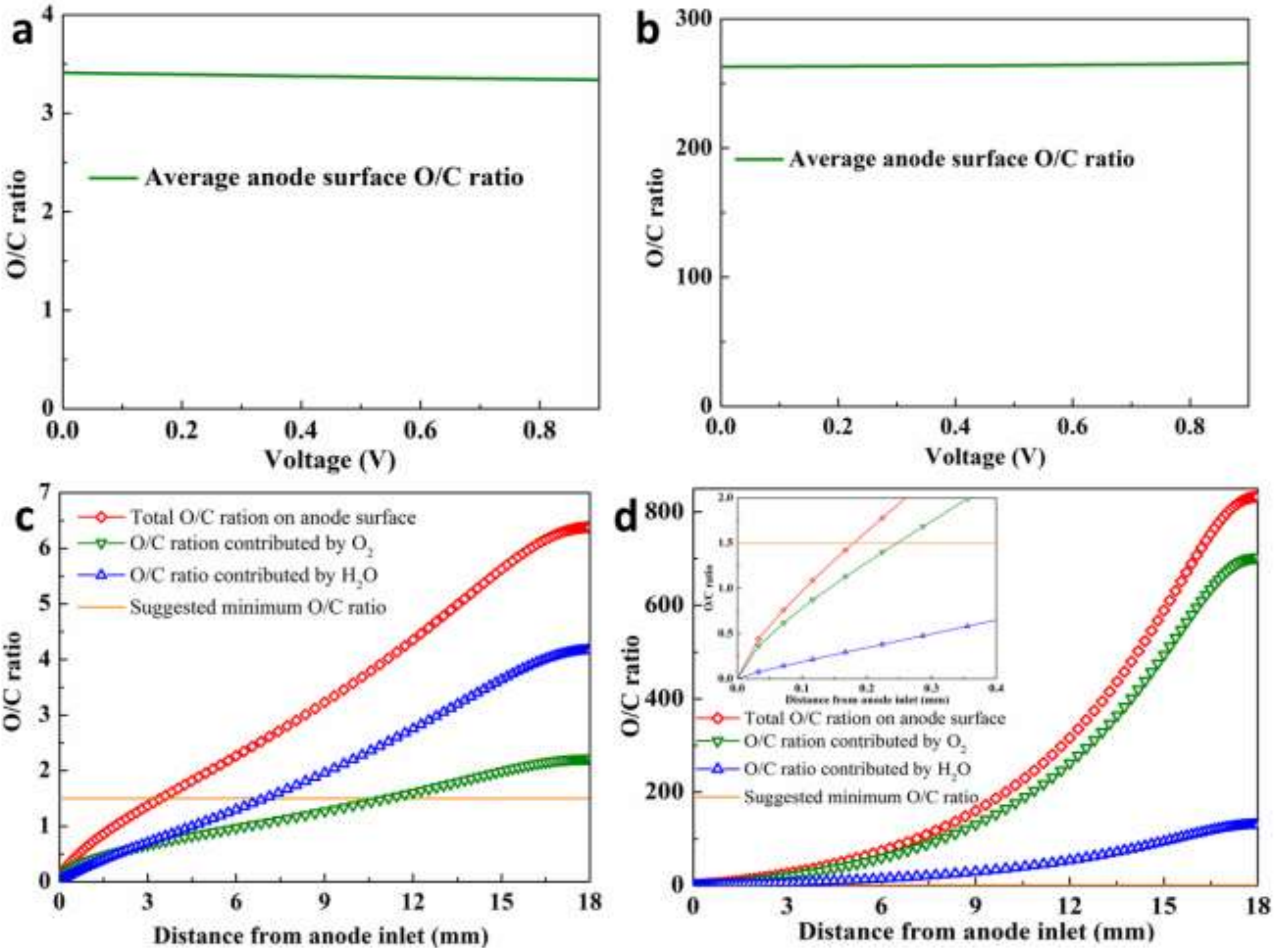

Fig. 4 The average anode surface O/C ratio of tubular AP-SOFCs at different operating potentials with 4 % CH_4 in anode inlet gas, 4 % (a) and 21 % (b) O_2 in cathode inlet gas; the breakdown of total O/C ration on anode surface along the cell length direction with 4 % CH_4 in anode inlet gas, 4 % (c) and 21 % (d) O_2 in cathode inlet gas at 0.45V operating potential.

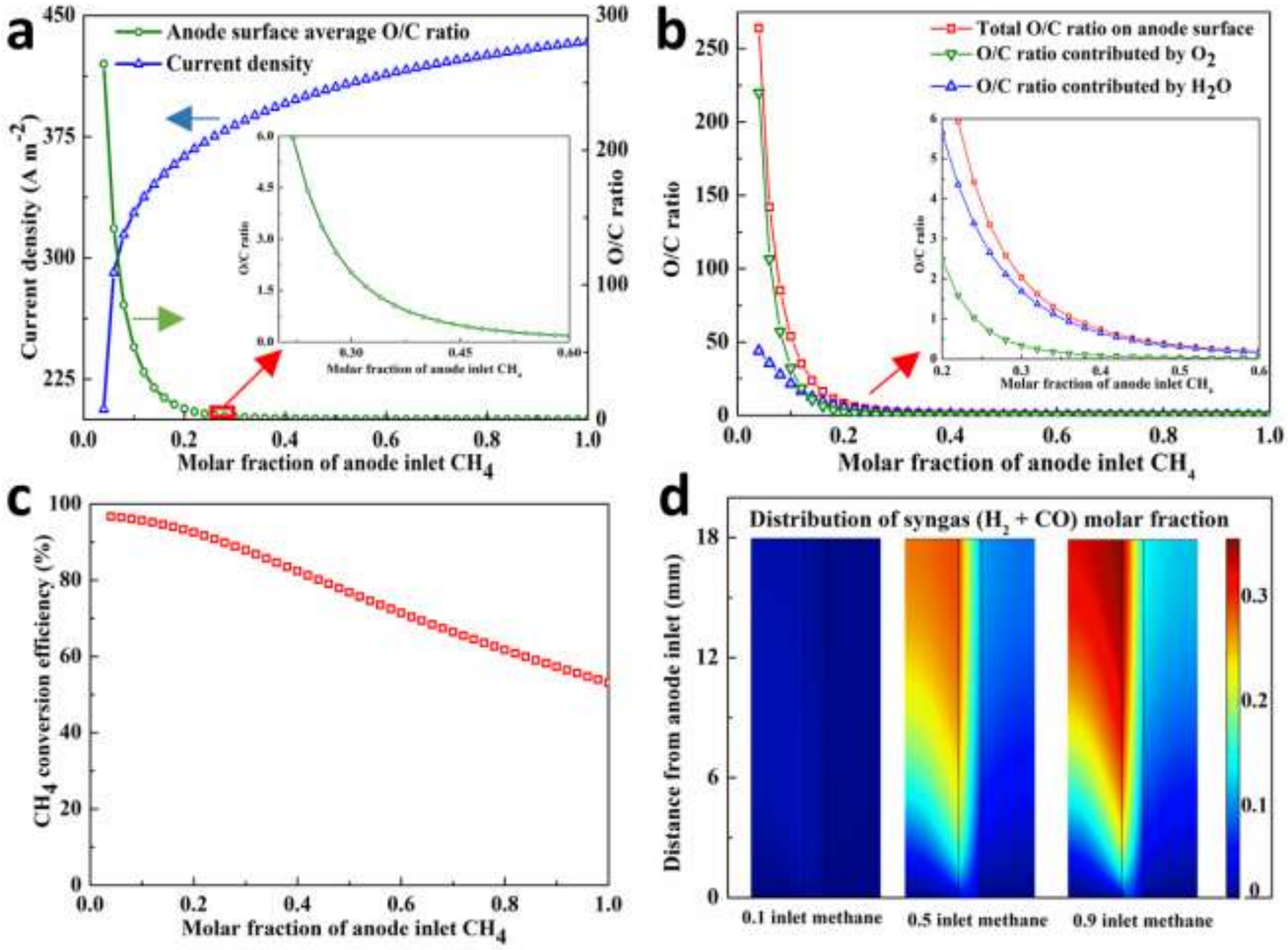

Fig. 5 The change of tubular AP-SOFC anode inlet CH_4 molar fraction on (a) anode surface average O/C ratio and current density at 0.45 V operating potential, (b) O/C ratio breakdown, (c) CH_4 conversion efficiency and (d) distribution of syngas with 0.1, 0.5 and 0.9 inlet CH_4 molar fraction.

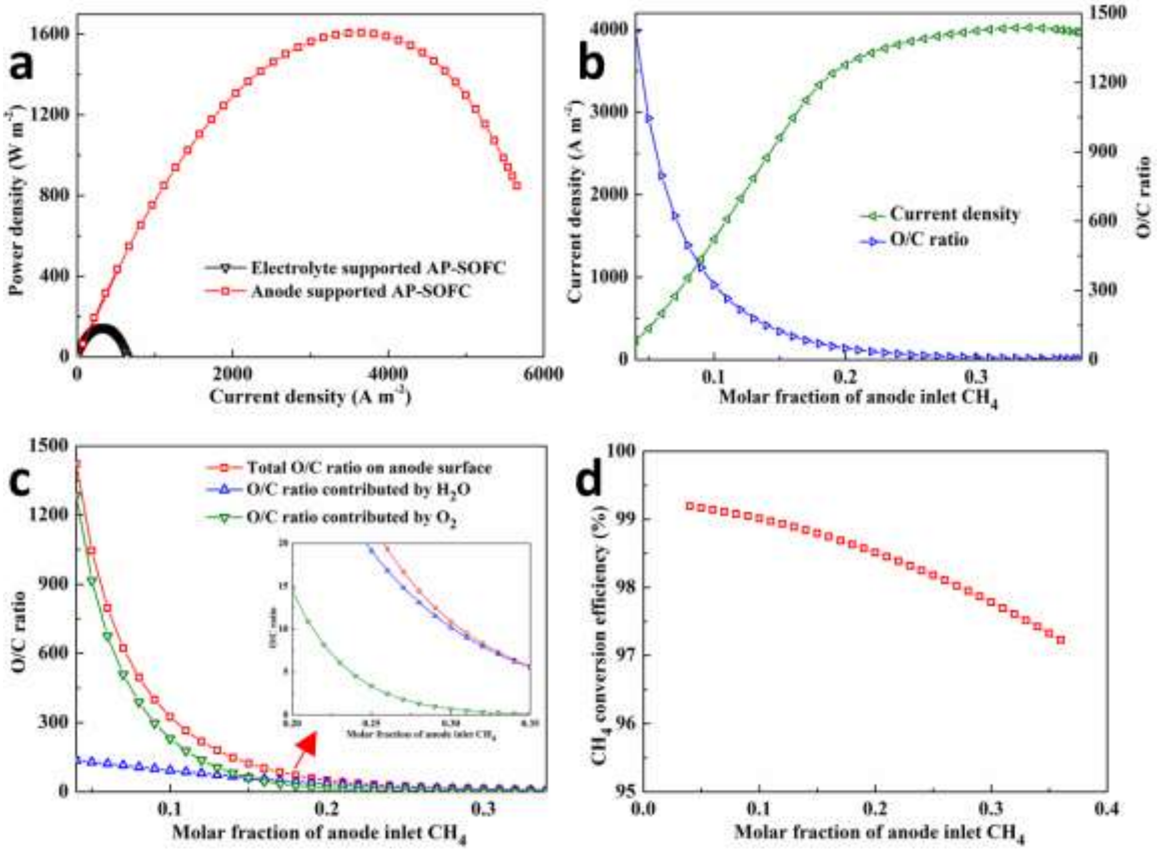

Fig. 6 (a)The comparison of electrolyte-supported and anode-supported AP-SOFCs on the output power density with 0.2 inlet CH_4 molar fraction; (b) the current density and O/C ratio characteristics with different inlet CH_4 molar fraction at 0.45 V operating potential (c) the breakdown of O/C ratio constitution and (d) the CH_4 conversion efficiency in anode-supported AP-SOFC at different anode inlet CH_4 molar factions.